Title

A fast and tiny current as common generator of slow regular pacemaking in brain and heart

Authors

Arthur Fyon[1], Oleksandra Pavlova[2], Nick Schaar[3], Pietro Mesirca[4], Julien Brandoit[1], Sofian Ringlet[5], Alessio Franci[1,6], Matteo E. Mangoni[4], Jochen Roeper[3], Guillaume Drion[1†], Vincent Seutin[2*†] & Kevin Jehasse[1*†]

Affiliations

[1]Neuroengineering laboratory, Montefiore Institute, University of Liège, Belgium.

[2]Laboratory of Neurophysiology, GIGA Institute, University of Liège, Belgium.

[3]Institute of Neurophysiology, Neuroscience Center, Goethe University, Frankfurt am Main, Germany.

[4]Institut de Génomique Fonctionnelle, Université de Montpellier, CNRS, INSERM, France.

[5]Laboratory of Molecular Regulation of Neurogenesis, GIGA Institute, University of Liège, Belgium.

[6]WEL-T Department, WEL Research Institute, Belgium.

[†]denotes equal contribution

*Corresponding authors. Email: v.seutin@uliege.be – kevin.jehasse@uliege.be

Abstract

Slow pacemaking is a key physiological process in specific excitable cells, yet its underlying mechanisms remain debated. Here we identify a conserved, voltage-dependent pacemaker current that is essential for slow, regular firing in both midbrain dopaminergic neurons and sinoatrial node cells. Conductance-based models incorporating this current reproduce stable pacemaking, requiring a fast-activating, small-amplitude current. This is further confirmed by dynamic-clamp experiments in dopaminergic neurons. Replacing the pacemaker current in a model with a voltage-independent conductance such as the non-selective sodium leak channels fails to sustain slow rhythmicity, highlighting the necessity for an adequate voltage dependence. Our results suggest a novel and shared biophysical mechanism for slow pacemaking in neuronal and cardiac systems.

Introduction

Pacemaking activity is a fundamental property of a subset of excitable cells that underpins vital rhythmic functions across biological systems. Pacemaker cells can be classified, based on the firing frequency, as either fast or slow pacemakers. While the mechanism to sustain fast pacemaking is known (*1*), slow pacemaking remains controversial. It has been suggested that it originates from the balanced interplay between several depolarizing and hyperpolarizing currents (*2*–*5*). The main currents involved are due to hyperpolarization-activated cyclic nucleotide-gated (HCN sustaining I_H in neurons and I_F in cardiac cells) and voltage-gated Ca^{2+} (Ca_v) channels, on the one hand, and A-type fast inactivating K^+ channels (I_A), on the other hand. Yet, experimental data shows that blocking or altering any of these channels does not eradicate slow pacemaking, although both its frequency and regularity can be affected (*3*, *6*–*9*). Another hypothesis is that the production of such a precise (coefficient of variation below 5%) and robust low frequency (1-5 Hz on average) pacemaking needs the reliable activation of a pacemaker current (I_{pace}) during the interspike interval (*1*, *6*, *10*, *11*) . Yet the nature, dynamics, and origins of such an essential current have remained elusive to date.

Recently, we found that a compound previously shown to block gating pore currents, 1-(2,4-xylyl)guanidinium (XG), eradicates the pacemaking activity of rodent midbrain dopamine neurons (mDANs) (*6*). Using voltage ramps and pacemaker-clamp, we were able to isolate the tiny current blocked by XG, reminiscent of the elusive I_{pace}. Since slow pacemaking is such a fundamental behavior for life, we hypothesized that this mechanism is conserved across neuronal and cardiac pacemaker cells and species. We therefore investigated whether similar effects of XG would be observed in human mDANs and in rodent sinoatrial node (SAN) cells and found it to be the case. Dynamic-clamp experiments, in which electrophysiological recordings are coupled to exogenous current injections to either add or subtract conductances, confirmed that XG-sensitive I_{pace} is necessary and sufficient for slow pacemaking. Next, we used both a conductance-based model of a mDAN (*12*) and a reduced neuronal model and showed that the voltage dependence of I_{XG} is ideally suited to be the effector of slow pacemaking. Taken together, our data supports the hypothesis of a conserved mechanism for slow pacemaking, encompassing neuronal and cardiac cells.

Results

Evidence for a shared mechanism of slow pacemaking across species and systems

We had previously shown that pacemaking of rodent mDANs is blocked by XG and had isolated the underlying current (**Fig. 1A-C**) (*6*). We first asked whether pacemaking in human mDANs derived from two different induced pluripotent stem cells (hIPSCs) lines (see Methods) would be similarly affected by the drug. These neurons were identified as mDANs based on their spontaneous slow firing frequency, hyperpolarization by dopamine and, in some cases, the expression of tyrosine hydroxylase (**Fig. S1**; see Methods). Upon superfusion of XG, their spontaneous activity was silenced (2.28 ± 0.44 Hz in control vs 0.12 ± 0.05 in XG, n = 9, p = 0.0039, Wilcoxon test; **Fig. 1D, E**), similarly to what we had observed in rodent models. In particular, as in rodent mDANs, the silencing of the electrical activity by XG does not involve a hyperpolarization, contrary to what is seen with dopamine, which is known to open G-protein-coupled inwardly rectifying channels in these cells (**Fig. S1**). Moreover, we observed a current sensitive to XG in human mDANs which is similar the one observed in rat mDANs (**Fig. 1F**). Taken together, these results suggest that the mechanism of pacemaking is conserved across species in this cell type.

To investigate whether this finding could be extended to another cell type, we next explored the case of SAN cells of the heart, which are also slow (1-5 Hz), very regular, pacemakers. In addition, similar to mDANs, these cells express high levels of L-type $Ca_v1.3$ channels and HCN channels (*13*). Upon superfusion of XG, we observed a marked decrease of the pacemaking activity in SAN cells (from 166.5 ± 9.1 bpm in control to 24.5 ± 10.1 bpm in XG, n = 11, p = 0.001, Wilcoxon test ; **Fig. 1G, H**). The silencing effect of XG was not due to its interaction with K^+ or Ca_v channels, nor with HCN channels (**Fig. S2**), but due to the inhibition of a pacemaker current (named I_{pace} hereafter) that had similar characteristics to those previously observed in mDANs (**Fig. 1I, J**). Interestingly, I_{pace} starts operating around -50 mV and its amplitude increases up to ~-20 mV, a voltage more depolarized than the threshold of the action potential in both cell types. Taken together, this data is strongly suggestive of a shared mechanism for slow pacemaking in mDANs and in SAN cells.

Modeling the pacemaker current confirms its ability to sustain slow pacemaking

We used a well-established conductance-based model to study slow pacemaking (*12*). Since this model is set to pace steadily without a pacemaker current, it relies on shifting

103 the activation curve of Na^+ (g_{Na}) and L-type Ca^{2+} (g_{CaL}) conductances to artificially
104 hyperpolarized potentials. We adjusted these activation curves to their measured
105 physiological values in mDANs (*14*, *15*) (**Fig. S3C**), which led to a loss of spontaneous
106 firing and a shift from type I to type II excitability (**Fig. S3B**). We then modeled the
107 pacemaker conductance (g_{pace}) from the current-voltage curve of the XG-sensitive I_{pace}
108 (**Fig. S3D**) and implemented it into the adjusted model (**Fig. S3E**). We were able to
109 recover a pacemaking activity with a voltage range of activation of g_{pace} similar to what
110 had been observed experimentally (**Fig. 2B**) (*6*), as well as to recover type 1 excitability
111 **(Fig. S3B**). Currentscape analysis (*16*) revealed the crucial contribution of g_{pace} during
112 pacemaking (**Fig. 2A**). We then measured the total current between two spikes and
113 observed that the resulting current is driven by g_{pace} (**Fig. 2B**) and has a small
114 amplitude similar to previous experimental observations in mDANs (*17*). Finally, we
115 measured the charge transfer of each conductance during the interspike interval and
116 the full period of the simulation (**Fig. 2C**). Interestingly, the transfer charge of g_{pace} (-
117 190.76 fC) is smaller than the other conductance such as g_{CaL} (-1457.89 fC) or H-type
118 conductance (g_H) (-2077.48 fC) during the interspike interval. Overall, these data
119 highlight the essential role of the small conductance g_{pace} in slow pacemaking.
120 We next investigated the dynamical range of g_{pace} which is necessary to maintain a
121 steady low frequency spontaneous activity (**Fig. 2D**). We explored both the density and
122 activation time constant of g_{pace}, relative to the activation of Na_v channels, and found
123 that the model remains stable as long as the activation of g_{pace} is very fast, close to
124 instantaneous. Moreover, g_{pace} can have a wide range of densities, making the
125 phenomenon robust. To verify that these observations are not limited to the particular
126 parameters used, we perfomed the same analysis using random parameters in which
127 slow pacemaking can be observed (**Fig. S4**). In all cases, we observed similar
128 requirements for the parameters of g_{pace}. Moreover, the addition of g_{pace} into the model
129 increased ion channel degeneracy (**Fig. S5**), especially for g_{Na} and g_{CaL}, suggesting
130 that it may normalize neuronal output in the face of biological variability (*18–21*).
131 To further explore the structure of this increased degeneracy, we performed principal
132 component analysis on the pacemaking solutions of the adjusted model. The analysis
133 revealed no preferred direction of variability, indicating that the contribution of g_{pace}
134 does not impose a dominant constraint on the system but instead distributes flexibility
135 across all conductances (**Fig. S5C**). This isotropic degeneracy suggests that slow

136 pacemaking remains robust even when the underlying ion channel expression varies
137 extensively, emphasizing the stabilizing role of g_{pace} in maintaining reliable activity.
138 Next, we used the dynamic-clamp approach to test how g_{pace} regulates slow
139 pacemaking in spontaneously active DANs from *substantia nigra pars compacta* (*SNc*)
140 (**Fig. 3A**). First, we injected several values of negative conductance and evaluated the
141 percentage of decrease in firing frequency (**Fig. 3B**). We observed a frequency
142 decrease of 50% at -0.06 nS and complete silencing at -0.3 nS (1.54 Hz (interquartile
143 range: 1.19 – 1.86 Hz) in ctrl vs. 0 Hz (interquartile range: 0) with g_{pace} = - 0,3 nS, n =
144 20, N = 3, p = <0,0001, Wilcoxon test ; **Fig 3B**). Injecting positive values for g_{pace}
145 increased the firing frequency as expected, leading to a depolarization block at the
146 highest value tested (above 0.3 nS, **Fig. 3C**). Finally, we preincubated *SNc* DANs with
147 XG to silence their activity and injected positive g_{pace} in order to test whether we are
148 able to rescue slow pacemaking (**Fig. 3D**). Overall, the rescue was successful in all
149 trials (n = 11) at a variable intensity of g_{pace} which is to be expected because of the
150 diversity in the mDAN population (*22*). The latter experiment demonstrates that our
151 modeling and experimental data are perfectly congruent.
152
153 *Requirements for slow pacemaking*
154 We next sought to understand how important g_{pace} is for slow pacemaking. We reduced
155 our conductance-based model to a minimal one, keeping only g_{Na} and g_{Kd} for spike
156 generation, g_{LNS} (leak conductance) to set the membrane at the desired potential.
157 Adding g_{pace} in this minimal configuration allows slow pacemaking similarly to our
158 complete model (**Fig. 4A**). In this model, slow pacemaking is still maintained with fast
159 activating g_{pace} over a wide range of densities, from 4.5 mS/mm² to 35.5 mS/mm² (**Fig.
160 4B**). Since our data shows that minimal configuration is sufficient to create slow
161 pacemaking, we investigate the role of the other conductances, especially A-type K^+
162 (g_{KA}), H-type (g_H) and Ca^{2+}-dependent K^+ (g_{KSK}) conductances. They have been shown
163 in slices to help maintaining the firing frequency and regularity constant during
164 membrane potential changes caused by excitatory and inhibitory inputs (*3*, *17*, *23*). We
165 introduced current noise in our minimal model and observed that the pacemaking
166 becomes irregular (**Fig. 4C**). In our complete model, the firing frequency is robust to
167 current injection, similarly to what have been observed by others (*3*, *17*, *23*). Moreover,
168 we also observed that these conductances, and especially g_{KSK}, help to reduce the
169 slope of the firing frequency – injected current relationship, which is expected.

170 We then challenged the requirement of a voltage-gated activation for g_{pace} in order to
171 obtain slow pacemaking. We replaced g_{pace} by a linear leak conductance similar to
172 NALCN channels (g_{Nalcn}), as they had been suggested to be the main drive of
173 pacemaking in mDANs (*10*, *24–26*). g_{Nalcn} failed to sustain slow pacemaking (**Fig. S6**).
174 In fact, low or high density of g_{Nalcn} could not generate spontaneous firing (**Fig. S6B**),
175 while activity could be observed in a small window of density, going from type II
176 excitability to fast pacemaking type I excitability. Our data therefore supports the notion
177 that slow pacemaking requires a current with a specific voltage-dependent activation
178 during the interspike interval, not a linear one.
179

180 **Discussion**

181 Slow pacemaking is a unique property which is observed in a subset of cells that play
182 a major role in rhythmic biological processes. However, its exact mechanism is still
183 controversial. Recently, we found that XG inhibits the pacemaking of rodent mDANs
184 and were able to isolate the current blocked by this compound (*6*). Here we show that
185 this effect can be extended to human mDANs and to mouse SAN cells. Remarkably,
186 the XG-sensitive conductance or g_{pace} has very similar voltage-dependence in mDANS
187 and SAN cells, starting to operate at ~-50 mV and slowly increasing in amplitude
188 towards more depolarized potentials. In our minimal conductance-based model, we
189 show that such voltage dependence is able to generate slow pacemaking, whereas
190 addition of a linear conductance such as NALCN is unable to induce this firing pattern.
191 In our adjusted conductance-based model of a mDAN, we show that addition of g_{pace}
192 is able to induce biologically realistic pacemaking. The properties of g_{pace} allows to
193 extend ion channel degeneracy, which makes our model more robust to biological
194 variability (**Fig. S5**). In this work, we describe key properties that I_{pace} should have.
195 First, its activation should be fast. Second, its amplitude can vary within a relatively
196 large range, which guarantees robustness. In our minimal model, we show that the
197 largest conductances, such as g_{CaL}, g_{KA} or g_H are not required for slow pacemaking (*3*,
198 *6*), but that I_{pace} is equally able to generate this rhythm.
199 Dynamic-clamp experiments confirmed the importance of g_{pace} (**Fig. 3**). Moreover, the
200 range of conductances to either rescue slow pacemaking upon XG perfusion or to
201 silence the neurons was a small fraction of the cell conductance, around 3 nS
202 measured in mDANs (*6*). Overall, 0.3 nS was enough in both conditions, confirming
203 the fact that pacemaking relies on a tiny current. These data support our hypothesis

that the pacemaker channel should have a unitary conductance value in the fS range (*6*, *11*). In fact, if g_{pace} were to have a single channel conductance similar to Na_v channels (around 20 pS), it would imply that slow pacemaking is sustained by at most 15 channels. Because of stochasticity, it will lead to very irregular firing in neurons and in the heart.

In mDANs, the role of several ion channels in pacemaking has been investigated over the years. L-type Ca_v channels were considered, since their pharmacological blockade with high concentrations of dihydropyridines silenced these neurons (*27–29*). However, these data were not observed using lower, pharmacologically relevant concentrations (*6*, *7*, *30*, *31*), therefore suggesting an off-target effect of dihydropyridines at high concentrations. We also confirm that in this study, as our minimal model runs without a Ca_v conductance. These channels are now considered as a linear amplifier of the firing frequency in mDANs (*7*). NALCN channels were also considered as they are expressed in most rhythmic neurons (*32*). Further studies showed controversial results, in which NALCN gene deletion or pharmacological blockade suppressed (*24–26*, *33*) or did not impact pacemaking activity (*6*, *25*). Our simulations show that a linear depolarizing conductance is unlikely to sustain stable and slow pacemaking (**Fig. S6**).

On the other hand, SAN cell pacemaking has been linked to either Ca^{2+}-linked processes or HCN channel activity (*34*). In the Ca^{2+} clock theory, L-type $Ca_v1.3$ channels are responsible for the main entry of Ca^{2+}, which is then pumped by SERCA pumps in the sarcoplasmic reticulum or by the Na^+/ Ca^{2+} exchanger NCX outside the cell. The genetic removal of $Ca_v1.3$ channels (*35*) or HCN channels (*36*) leads to arrhythmia, but not to a silenced activity. On the other hand, XG does silence pacemaking in these cells by blocking a current that is highly similar to the one found in mDANs. This observation clearly opens up a new hypothesis on cardiac pacemaking that is more consistent with previous experimental results than the current theories.

In conclusion, we shed new light on the controversial mechanism of slow pacemaking in excitable cells and, importantly, demonstrate a commonality across systems, an observation that is very novel and surprising.

Materials and Methods

Modeling

Programming language

The Julia programming language was used in this work (37). Numerical integration was realized using *DifferentialEquations.jl*. Fitting was realized using *LsqFit.jl*. PCA was realized using *MultivariateStats.jl*.

Equation 1:

$$C\dot{V} = -\bar{g}_{Na}\, m^3\, h\, h_s\, (V - E_{Na}) - \bar{g}_{CaL}\, l\, (V - E_{Ca}) - \bar{g}_{Kd}\, n^3\, (V - E_K)$$
$$- \bar{g}_{KA}\, p\, \left(\frac{q_1}{2} + \frac{q_2}{2}\right) (V - E_K) - \bar{g}_{KERG}\, o\, (V - E_K)$$
$$- \frac{\bar{g}_{KSK}}{1 + \left(\frac{0.00019}{[Ca^{+2}]}\right)^4} (V - E_K) - \bar{g}_H\, m_H^2\, (V - E_H) - g_{LCa}\, (V - E_{Ca})$$
$$- g_{LNS}\, (V - E_{LNS}) + \frac{100\, I_{app}}{\pi\, d\, L}$$

Here, the dot notation represents time derivative (in /ms), V is the membrane potential (in mV), and C the membrane capacitance (in µF/cm²). The ionic currents are: I_{Na} (transient sodium), I_{CaL} (L-type calcium), I_{Kd} (delayed rectifier potassium), I_{KA} (A-type potassium), I_{KERG} (ether-à-go-go potassium), I_{KSK} (SK potassium), I_H (hyperpolarization-activated current), I_{LCa} (calcium leak), and I_{LNS} (non-specific leak). Reversal potentials are denoted by E. The intracellular calcium concentration $[Ca^{+2}]$ follows voltage-dependent kinetics as in (*13*). The soma geometry is defined by its diameter d and length L (in µm). The applied current is I_{app} (in pA).

Maximal conductances are denoted by the bar notation (in mS/cm²), representing the channel conductance when fully open. Gating variables follow first-order voltage-dependent kinetics of the following form.

Equation 2:

$$\tau_x(V)\, \dot{x} = x_\infty(V) - x$$

Here, x is the gating variable, $\tau_x(V)$ its voltage-dependent time constant, $x_\infty(V)$ its steady-state activation or inactivation function. Variables that were adjusted in this work are specified in the following section.

Unless otherwise stated, the original model parameters were used (Table S1) (*13*).

$$\bar{g}_{Na} = 6;\ \bar{g}_{CaL} = 0.139;\ \bar{g}_{Kd} = 1.117;\ \bar{g}_{KA} = 1.68;\ \bar{g}_{KERG} = 0.13;$$
$$\bar{g}_{KSK} = 0.07;\ \bar{g}_H = 0.078;\ g_{LCa} = 0.00245;\ g_{LNS} = 0.28;$$
$$C = 1;\ E_{Na} = 60; E_K = -90; E_{Ca} = 50; E_H = -29; E_{LNS} = -65; d = 15; L = 25$$

Adjustment of the mDAN conductance-based model and fitting of the pacemaking current

Before introducing the pacemaking current, activation of the transient sodium and L-type calcium channel was realized. In the original model (*13*), the steady-state activation functions were defined as follows.

Equation 3:

$$m_\infty(V) = \frac{1}{1 + e^{-\frac{V+30.09}{13.2}}};\ l_\infty(V) = \frac{1}{1 + e^{-\frac{V+45}{7.5}}}$$

These sigmoidal functions have half-activation voltages of −30.09 mV and −45 mV, respectively, which are substantially more hyperpolarized than values reported experimentally. In the adjusted model, both activation curves were shifted to −10 mV. The ultraslow inactivation of the transient sodium current (h_s) was disabled, as it was an adjustment to generate slow pacemaking in the original model (*12*).

The pacemaking current was fitted to a previously published voltage–current relationship (*3*) (**Fig. 1C**). The pacemaking current was modeled as a non-inactivating current, which provided an accurate fit without unrealistic parameter estimates.

Equation 4:

$$\begin{cases} I_{pace} = \bar{g}_{pace} m_{pace} \left(V - E_{pace}\right) \\ \tau_{m,pace}(V)\, \dot{m}_{pace} = m_{pace,\infty}(V) - m_{pace} \\ m_{pace,\infty}(V) = \dfrac{1}{1 + e^{-\frac{V - V_{half}}{V_{slope}}}} \end{cases}$$

Because the fit was performed on steady-state voltage–current data, no biological information was available on the time constant of pacemaking activation. We therefore set

Equation 5:

$$\tau_{m,pace}(V) = \alpha \cdot \tau_m(V)$$

where $\tau_m(V)$ is the activation time constant of the transient sodium current.

Fitting yielded the following parameter values, given to one decimal place.

$$\bar{g}_{pace} = 6.5;\ V_{half} = -13.3;\ V_{slope} = 6;\ E_{pace} = 4.3$$

Since this pacemaking conductance corresponds to a specific neuron, it was varied throughout the study to test robustness rather than fixed at the fitted value. Unless otherwise stated, the following parameters were used in the adjusted model.

$$\bar{g}_{Na} = 25;\ \bar{g}_{CaL} = 1;\ \bar{g}_{Kd} = 10;\ \bar{g}_{KA} = 1.68;\ \bar{g}_{KERG} = 0.13;\ \bar{g}_{KSK} = 0.3;$$

$$\bar{g}_{H} = 0.078;\ g_{LCa} = 0.00245;\ g_{LNS} = 0.28;\ \bar{g}_{pace} = 5;$$

$$C = 1;\ E_{Na} = 60; E_{K} = -90; E_{Ca} = 50; E_{H} = -29; E_{LNS} = -65; d = 15; L = 25$$

Modeling of a NALCN current

In **Fig. 4C-E**, the NALCN conductance was modeled as a voltage-independent sodium current.

Equation 6:

$$I_{NALCN} = g_{NALCN}\,(V - E_{Na})$$

Degenerate population building

In **Fig. S5**, two degenerate populations (N=200) exhibiting pacemaking were generated for the original and adjusted models. The procedure was identical for both populations. All ionic conductances were randomly assigned using a uniform distribution between 0 and an upper bound value, corresponding to the ordinates of **Fig. S5B**. Each model was simulated and retained in the population if its firing frequency was between 1 and 5 Hz, if the spike peak exceeded 0 mV, and if the minimum membrane potential was between −90 and −60 mV.

<u>Cell Culture</u>

Cell lines

Two human induced pluripotent stem cell (hiPSC) lines were used in this study: GM23338 (gift from Prof. Ira Mercedes Espuny Camacho, GIGA Neurosciences, University of Liège) and a human TH-reporter iPSC line expressing mCherry (gift from Dr. Aleksandar Rakovic, Institute of Neurogenetics, University of Lübeck) (*38*). Prior to differentiation, cells were maintained for 2–3 consecutive passages in E8 medium using standard EDTA-based passaging when confluency reached 70–80%.

Differentiation to midbrain dopaminergic neurons

332 Differentiation was carried out using a slightly modified version of the protocol
333 published by Stathakos et al. (2019) (*39*). Briefly, hiPSCs were cultured in E8 medium
334 for up to 4 days before switching to neural induction medium consisting of N2B27
335 supplemented with 100 nM LDN193189, 10 µM SB431542, 300 ng/mL SHH, and 0.6
336 µM CHIR99021. This was considered neuralization day 0. Cells were passaged on
337 polyornithine/laminin-coated plates at days 3 and 7 using Accutase at a density of 4 ×
338 10^4 cells/cm² in induction medium with 10 µM Y27632 or 1:100 RevitaCell.
339 From day 11, the medium was replaced with progenitor expansion medium (N2B27
340 with 20 ng/mL BDNF, 20 ng/mL GDNF, 0.2 mM ascorbic acid, and 10 µM Y27632).
341 Upon confluence, cells were passaged every 3-4 days in this medium. Terminal
342 differentiation started on day 16 by seeding cells at 5,000 cells/cm² onto PO/laminin-
343 coated coverslips in N2B27 supplemented with 20 ng/mL BDNF, 20 ng/mL GDNF, 0.2
344 mM ascorbic acid, 500 µM db-cAMP, 10 µM DAPT, and 10 µM Y27632. Cells were
345 allowed to attach for ~1 hour before flooding wells with the same medium. Media was
346 refreshed every 3 days with 50% volume exchange.
347
348 Tissue preparation
349 *Animals*
350 For dynamic-clamp experiments, adult male C57BL/6N (Charles River Laboratories)
351 mice (8 to 14 weeks of age) were used. A maximum of 5 mice were housed per cage
352 and single animal housing was avoided when possible. Animals were maintained on a
353 12-hour light-dark cycle and provided with water and food ad libitum. All experimental
354 procedures involving mice were approved by the German Regional Council of
355 Darmstadt.

356 For SAN cells experiments, the study is in accordance with the Guide for the Care and
357 Use of Laboratory Animals published by the US National Institute of Health (NIH
358 Publication No. 85-23, revised 1996) and European directives (2010/63/EU). All mice
359 used were from the C57BL/6J background (Charles River and Janvier labs).
360 Experimental procedures were approved by the Ethical Panel of the University of
361 Montpellier and the French Ministry of Agriculture (protocol no: 2017010310594939).
362 Animals were housed in the IGF animal facility with free access to food and water and
363 were exposed to 12 h light/dark cycles in a thermostatically controlled room (21–22 °C)
364 with 40−60% humidity.

365

366 *Slice preparation for mouse midbrain dopamine neurons*

367 Animals were anesthetized by intraperitoneal injection of ketamine (250 mg/kg;
368 Ketaset, Zoetis) and medetomidine hydrochloride (2.5 mg/kg; Domitor, OrionPharma)
369 before intracardial perfusion using ice-cold ACSF consisting of the following: 50 mM
370 sucrose, 125 mM NaCl, 2.5 mM KCl, 25 mM $NaHCO_3$, 1.25 mM NaH_2PO_4, 2.5 mM
371 glucose, 6 mM $MgCl_2$, 0.1 mM $CaCl_2$, and 2.96 mM kynurenic acid (Sigma-Aldrich),
372 oxygenated with 95% O_2 and 5% CO_2. Rostral coronal midbrain slices (bregma, −2.92
373 to −3.16 mm) were sectioned into 250-µm slices using a vibrating blade microtome
374 (VT1200s, Leica). Before the experiment, slices were kept at 37°C for 1 hour in
375 oxygenated extracellular solution containing the following: 22.5 mM sucrose, 125 mM
376 NaCl, 3.5 mM KCl, 25 mM $NaHCO_3$, 1.25 mM NaH_2PO_4, 2.5 mM glucose, 1.2 mM
377 $MgCl_2$, and 1.2 mM $CaCl_2$.

378 *Mouse sinoatrial node cell isolation*

379 Sinoatrial node myocytes were isolated as previously described (*40*). Briefly, Sinoatrial
380 tissue (SAN) strips were immersed into "low Ca^{2+}" Tyrode's solution containing (in
381 mM): 140 NaCl, 5.4 KCl, 0.5 $MgCl_2$, 1.2 KH_2PO_4, 50 taurine, 5.5 D-glucose, 1 mg/mL
382 BSA, and 5 Hepes (adjusted to pH 6.9 with NaOH) for 5 min. The tissue was then
383 transferred into the low-Ca^{2+} solution containing Liberase TH (0.15 mg/mL, Roche) and
384 Elastase (0.48 mg/mL, Worthington). Digestion was carried out for 15-20 min at 36 °C.
385 SAN strips were then washed in "Kraftbrühe" (KB) solution containing 100 L-glutamic
386 acid potassium salt, 10 L-Aspartic acid potassium salt, 25 KCl, 80 KOH, 10 KH_2PO_4, 2
387 $MgSO_4$, 5 Creatine, 0.5 EGTA, 20 D-glucose, 20 taurine, 1 mg/mL BSA, and 5 Hepes
388 (adjusted to pH 7.2 with KOH). Single myocytes were isolated from the SAN tissue by
389 manual agitation using a flame-forged Pasteur's pipette in KB solution at 36 °C. For
390 recovering of pacemaker activity, Ca^{2+} was gradually reintroduced into the cells'
391 storage solution to a final concentration of 1.8 mM. Cells were then stored at room
392 temperature until use.

393

394 <u>Electrophysiological Recordings</u>

395 *Midbrain dopamine neurons*

396 For rat mDANs, the recordings were obtained from previous work (*6*)

397 For human mDANs, electrophysiological properties of differentiated neurons were
398 assessed using both on-cell and whole-cell patch-clamp recordings performed at 30°C
399 with a Multiclamp 700B amplifier and Clampex 11.1 software. The extracellular solution
400 contained (in mM): 140 NaCl, 5 KCl , 2 $CaCl_2$,2 $MgCl_2$,15 HEPES, and 10 D-glucose;
401 pH was adjusted to 7.3 with NaOH. The intracellular pipette (3-5 MΩ) solution
402 contained (in mM): 135 K-gluconate, 10 NaCl, 0.5 $CaCl_2$, 15 HEPES, 2 Na_2ATP, and
403 5 EGTA; pH adjusted to 7.3 with KOH, osmolarity ~ 300 mosm. Putative *substantia*
404 *nigra pars compacta* (*SNc*)-type mDANs were identified by similar characteristic
405 electrophysiological features we used to identify rodent mDANs (*6*, *41–43*), including
406 spontaneous pacemaking activity (0.5–5 Hz), action potential duration > 1.35 ms
407 (measured at half-amplitude), a prominent hyperpolarization-activated inward current
408 (I_H), and membrane hyperpolarization > 5 mV in response to 100 μM dopamine from a
409 holding potential of -60 mV. I_H was observed in many, but not all neurons sastifying
410 these criteria. To test the inhibition of pacemaker activity, 600 μM of 1-(2,4-
411 xylyl)guanidinium mesylate (XG) was applied to the bath solution. XG was produced
412 as previously described (*6*).
413 For dynamic-clamp recordings in mouse *SNc* DANs, slices were placed in a heated
414 recording chamber (37°C) that was superfused with the oxygenated extracellular
415 solution with a flow rate of 2 to 4 ml/min. CNQX (20 μM), DL-AP5 (10 μM), gabazine
416 (4 μM; SR95531), and were added to inhibit respectively excitatory and inhibitory
417 synaptic transmission. Neurons were visualized using infrared differential interference
418 contrast video microscopy with a digital camera (VX55, Till Photonics) connected to an
419 upright microscope (Axioskop 2, FSplus, Zeiss). Patch pipettes were pulled from
420 borosilicate glass (GC150TF-10, Harvard Apparatus, Holliston, MA, USA) using a
421 temperature controlled, horizontal pipette puller (DMZ-Universal Puller, Zeitz). Patch
422 pipettes (3 to 5 MΩ) were filled with a solution containing the following: 135 mM K-
423 gluconate, 5 mM KCl, 10 mM HEPES, 0.1 mM EGTA, 5 mM $MgCl_2$, 0.075 mM $CaCl_2$,
424 5 mM Na adenosine 5′-triphosphate, 1 mM Li guanosine 5′-triphosphate, and 0.1%
425 Neurobiotin, adjusted to a pH 7.35 with KOH. For pharmacology, slices were
426 preincubated for at least 10 min with XG mesylate (2 mM) before recording. Recordings
427 were performed using an EPC-10 patch-clamp amplifier (HEKA Elektronik) with a
428 sampling rate of 20 kHz and a low-pass filter (Bessel, 5 kHz). For analysis, recordings
429 were further digitally filtered at 1 KHz. A realtime Linux-based data acquisition program

430 (RTXI; http://rtxi.org) was used to inject online calculated currents (acquisition rates of
431 10 kHz) of the modelled XG-sensitive conductance according to the following equation:
432 *Equation 7*

433 $$\begin{cases} I_{pace} = \bar{g}_{pace} m_{pace} \left(V - E_{pace}\right) \\ \tau_{m,pace}\, \dot{m}_{pace} = m_{pace,\infty}(V) - m_{pace} \end{cases}$$

434

435 V is the membrane voltage in mV, E_{pace} the reversal potential in mV and g_{pace} is the
436 conductance in nS, according to fit the fit in **Fig.2A**.

437

438 *Mouse sinoatrial node cells*

439 SAN cells were harvested in custom-made chambers with glass bottoms for cell
440 attachment and superfused with Tyrode solution containing (in mM): 140 NaCl, 5.4
441 KCl, 1 $MgCl_2$, 1.8 $CaCl_2$, 5.5 D-glucose and 5 Hepes (adjusted to pH 7.4 with NaOH).
442 warmed at 36°C before recording.

443 XG-sensitive, delayed-rectifier potassium ($I_{K,r}$)and "funny" (I_F) currents were recorded
444 in extracellular Tyrode's solution under the standard whole-cell configuration whereas
445 action potentials were measured by perforated patch clamp technique with escin (0.04
446 mg/mL, Sigma-Aldrich) also in extracellular Tyrode's solution. For I_F recordings, 2 mM
447 $BaCl_2$ was added to Tyrode's solution to block $I_{K,1}$. Electrodes had a resistance of 3–
448 4 MΩ when filled with a solution containing (in mM): 80 K-aspartate, 50 KCl, 1 $MgCl_2$,
449 2 $CaCl_2$, 5 EGTA, 5 HEPES, and 3 ATP-Na (adjusted to pH 7.2 with KOH). Seal
450 resistances were in the range of 2–5 GΩ.

451 Superfusion of pre-warmed (36°C) experimental solutions was achieved by using a
452 multi-MPRE8 heating pen (Cell Micro Controls) and data acquisition was performed
453 using Multiclamp 700B patch-clamp amplifiers connected to a Digidata 1322A interface
454 (Molecular Devices, Saint Jose, CA, USA).

455

456 <u>Immunocytochemistry</u>

457 The DA phenotype of neurons in the process of maturation was confirmed by
458 immunocytochemistry as described earlier (*44*) with the use of tyrosine hydroxylase
459 (TH) (Merck, AB152) and βIII tubulin (TUBB3)/ TUJ1 (BioLegend, MMS-435P)
460 antibodies. Samples were imaged using an inverted confocal microscope (Leica SP5),
461 with a resolution of 512 x 512 pixels, pixel size is 0.758 µm. A ratio of TH+/TUBB3+

462 was measured by counting the number of TH+ or TUBB3+ cells, in order to assess the
463 maturation of the human mDAN culture (*44*).
464
465 Data analysis
466 Dynamic-clamp data was digitally filtered at 1 kHz and further exported as MAT-files
467 using Fitmaster (Heka Elektronik). Offline data analysis was performed using custom-
468 written scripts in MATLAB. Spike thresholds were determined using the first derivative
469 of the recording where dVm/dt ≥ 10 mV/ms. Spike thresholds, peaks and minima after
470 hyperpolarization potential were visually verified for each cell. The g_{pace}-modulated
471 firing frequency was averaged for the first three ISIs (frequency in Hz).
472 All statistical analysis were performed using GraphPad Prism 10.2.1. Non-parametric
473 Wilcoxon's tests were performed and data are reported as mean ± standard error of
474 the mean (SEM) and as median (interquartile range). Number of cells are denoted by
475 n, number of animals used as N.
476
477 **Supplementary Text**
478 *Specific parameter values used*
479 In **Fig. 4A-B**, the non-specific leak conductance was reduced to 0.01 to lower the firing
480 frequency.
481 In **Fig. S4**, ten sets of conductances were randomly chosen from the degenerate
482 population with a fixed random seed for reproducibility.
483 In **Fig. S6**, a NALCN conductance of 0.012 mS/cm^2 was used, and values of 0.004
484 mS/cm^2 and 0.012 mS/cm^2 were used for the FI curves in **Fig. S6C**. The CaL
485 conductance was reduced to 0.05 mS/cm^2 and the Kd conductance to 3 mS/cm^2 to
486 enlarge the firing region with respect to the NALCN conductance and facilitate
487 visualization.
488 **References**
489 1. B. P. Bean, Mechanisms of pacemaking in mammalian neurons. *J. Physiol.* **n/a**
490 (2024).

491 2. E. Marder, J.-M. Goaillard, Variability, compensation and homeostasis in neuron
492 and network function. *Nat. Rev. Neurosci.* **7**, 563–574 (2006).

3. J. Amendola, A. Woodhouse, M. F. Martin-Eauclaire, J. M. Goaillard, Ca 2+/cAMP-sensitive covariation of I A and I H voltage dependences tunes rebound firing in dopaminergic neurons. *J. Neurosci.* **32**, 2166–2181 (2012).

4. Y. Amarillo, E. Zagha, G. Mato, B. Rudy, M. S. Nadal, The interplay of seven subthreshold conductances controls the resting membrane potential and the oscillatory behavior of thalamocortical neurons. *J. Neurophysiol.* **112**, 393–410 (2014).

5. E. G. Lakatta, V. A. Maltsev, T. M. Vinogradova, A Coupled SYSTEM of Intracellular Ca2+ Clocks and Surface Membrane Voltage Clocks Controls the Timekeeping Mechanism of the Heart's Pacemaker. *Circ. Res.* **106**, 659–673 (2010).

6. K. Jehasse, L. Massotte, S. Hartmann, R. Vitello, S. Ringlet, M. Vitello, H. C. Chua, S. A. Pless, D. Engel, J.-F. Liégeois, B. Lakaye, J. Roeper, V. Seutin, The gating pore blocker 1-(2,4-xylyl)guanidinium selectively inhibits pacemaking of midbrain dopaminergic neurons. *Neuropharmacology* **197**, 108722 (2021).

7. J. Shin, L. Kovacheva, D. Thomas, S. Stojanovic, C. J. Knowlton, J. Mankel, J. Boehm, N. Farassat, C. Paladini, J. Striessnig, C. C. Canavier, G. Geisslinger, J. Roeper, Cav1.3 calcium channels are full-range linear amplifiers of firing frequencies in lateral DA SN neurons. *Sci. Adv.* **8**, eabm4560 (2022).

8. R. E. BoSmith, I. Briggs, N. C. Sturgess, Inhibitory actions of ZENECA ZD7288 on whole-cell hyperpolarization activated inward current (If) in guinea-pig dissociated sinoatrial node cells. *Br. J. Pharmacol.* **110**, 343–349 (1993).

9. E. E. Verheijck, A. C. G. van Ginneken, R. Wilders, L. N. Bouman, Contribution of L-type Ca2+current to electrical activity in sinoatrial nodal myocytes of rabbits. *Am. J. Physiol.-Heart Circ. Physiol.* **276**, H1064–H1077 (1999).

10. Z. M. Khaliq, B. P. Bean, Pacemaking in Dopaminergic Ventral Tegmental Area Neurons: Depolarizing Drive from Background and Voltage-Dependent Sodium Conductances. *J. Neurosci.* **30**, 7401–7413 (2010).

11. V. Seutin, K. Jehasse, G. Drion, An alternative mechanism for slow pacemaking. *J. Physiol.* **n/a** (2024).

12. N. Yu, C. C. Canavier, A Mathematical Model of a Midbrain Dopamine Neuron Identifies Two Slow Variables Likely Responsible for Bursts Evoked by SK Channel Antagonists and Terminated by Depolarization Block. *J. Math. Neurosci. JMN* **5**, 5 (2015).

13. M. E. Mangoni, J. Nargeot, Genesis and Regulation of the Heart Automaticity. *Physiol. Rev.* **88**, 919–982 (2008).

14. V. Seutin, D. Engel, Differences in Na+ conductance density and Na+ channel functional properties between dopamine and GABA neurons of the rat substantia nigra. *J. Neurophysiol.* **103**, 3099–3114 (2010).

15. P. Durante, C. G. Cardenas, J. A. Whittaker, S. T. Kitai, R. S. Scroggs, Low-Threshold L-type Calcium Channels in Rat Dopamine Neurons. *J. Neurophysiol.* **91**, 1450–1454 (2004).

16. L. M. Alonso, E. Marder, Visualization of currents in neural models with similar behavior and different conductance densities. *eLife* **8**, e42722 (2019).

17. Z. M. Khaliq, B. P. Bean, Dynamic, Nonlinear Feedback Regulation of Slow Pacemaking by A-Type Potassium Current in Ventral Tegmental Area Neurons. *J. Neurosci.* **28**, 10905–10917 (2008).

18. J.-M. Goaillard, E. Marder, Ion Channel Degeneracy, Variability, and Covariation in Neuron and Circuit Resilience. *Annu. Rev. Neurosci.* **44**, 335–357 (2021).

19. A. Fyon, A. Franci, P. Sacré, G. Drion, Dimensionality reduction of neuronal degeneracy reveals two interfering physiological mechanisms. *PNAS Nexus* **3**, pgae415 (2024).

20. G. Drion, T. O'Leary, E. Marder, Ion channel degeneracy enables robust and tunable neuronal firing rates. *Proc. Natl. Acad. Sci. U. S. A.* **112**, E5361–E5370 (2015).

548 21. T. O'Leary, A. H. Williams, A. Franci, E. Marder, Cell Types, Network
549 Homeostasis, and Pathological Compensation from a Biologically Plausible Ion
550 Channel Expression Model. *Neuron* **82**, 809–821 (2014).

551 22. J. Roeper, Dissecting the diversity of midbrain dopamine neurons. *Trends*
552 *Neurosci.* **36**, 336–342 (2013).

553 23. M. H. Higgs, J. A. Jones, C. J. Wilson, M. J. Beckstead, SK and Kv4 Channels
554 Limit Spike Timing Perturbations in Pacemaking Dopamine Neurons. *eNeuro* **10**
555 (2023).

556 24. F. Philippart, Z. M. Khaliq, Gi/o protein-coupled receptors in dopamine neurons
557 inhibit the sodium leak channel NALCN. *eLife* **7** (2018).

558 25. D. E. Cobb-Lewis, L. Sansalone, Z. M. Khaliq, Contributions of the Sodium Leak
559 Channel NALCN to Pacemaking of Medial Ventral Tegmental Area and
560 Substantia Nigra Dopaminergic Neurons. *J. Neurosci.* **43**, 6841–6853 (2023).

561 26. K. B. Um, S. Hahn, S. W. Kim, Y. J. Lee, L. Birnbaumer, H. J. Kim, M. K. Park,
562 TRPC3 and NALCN channels drive pacemaking in substantia nigra
563 dopaminergic neurons. *eLife* **10**, e70920 (2021).

564 27. M. Puopolo, E. Raviola, B. P. Bean, Roles of Subthreshold Calcium Current and
565 Sodium Current in Spontaneous Firing of Mouse Midbrain Dopamine Neurons.
566 *J. Neurosci.* **27**, 645–656 (2007).

567 28. S. Nedergaard, J. A. Flatman, I. Engberg, Nifedipine- and omega-conotoxin-
568 sensitive Ca2+ conductances in guinea-pig substantia nigra pars compacta
569 neurones. *J. Physiol.* **466**, 727–747 (1993).

570 29. C. S. Chan, J. N. Guzman, E. Ilijic, J. N. Mercer, C. Rick, T. Tkatch, G. E.
571 Meredith, D. J. Surmeier, 'Rejuvenation' protects neurons in mouse models of
572 Parkinson's disease. *Nature* **447**, 1081–1086 (2007).

573 30. G. Drion, L. Massotte, R. Sepulchre, V. Seutin, How Modeling Can Reconcile
574 Apparently Discrepant Experimental Results: The Case of Pacemaking in
575 Dopaminergic Neurons. *PLOS Comput. Biol.* **7**, e1002050 (2011).

576 31. J. N. Guzman, J. Sánchez-Padilla, C. S. Chan, D. J. Surmeier, Robust
577 Pacemaking in Substantia Nigra Dopaminergic Neurons. *J. Neurosci.* **29**,
578 11011–11019 (2009).

579 32. T. Z. Lu, Z.-P. Feng, NALCN: A Regulator of Pacemaker Activity. *Mol. Neurobiol.*
580 **45**, 415–423 (2012).

581 33. J. Wang, M. Su, D. Zhang, L. Zhang, C. Niu, C. Li, S. You, Y. Sang, Y. Zhang,
582 X. Du, H. Zhang, The cation channel mechanisms of subthreshold inward
583 depolarizing currents in the mice VTA dopaminergic neurons and their roles in
584 the chronic-stress-induced depression-like behavior. *eLife* **12**, RP88319 (2024).

585 34. E. G. Lakatta, D. DiFrancesco, What keeps us ticking: a funny current, a calcium
586 clock, or both? *J. Mol. Cell. Cardiol.* **47**, 157–170 (2009).

587 35. A. G. Torrente, P. Mesirca, P. Neco, R. Rizzetto, S. Dubel, C. Barrere, M.
588 Sinegger-Brauns, J. Striessnig, S. Richard, J. Nargeot, A. M. Gomez, M. E.
589 Mangoni, L-type Cav1.3 channels regulate ryanodine receptor-dependent Ca2+
590 release during sino-atrial node pacemaker activity. *Cardiovasc. Res.* **109**, 451–
591 461 (2016).

592 36. P. Mesirca, J. Alig, A. G. Torrente, J. C. Müller, L. Marger, A. Rollin, C.
593 Marquilly, A. Vincent, S. Dubel, I. Bidaud, A. Fernandez, A. Seniuk, B. Engeland,
594 J. Singh, L. Miquerol, H. Ehmke, T. Eschenhagen, J. Nargeot, K. Wickman, D.
595 Isbrandt, M. E. Mangoni, Cardiac arrhythmia induced by genetic silencing of
596 'funny' (f) channels is rescued by GIRK4 inactivation. *Nat. Commun.* **5**, 4664
597 (2014).

598 37. J. Bezanson, A. Edelman, S. Karpinski, V. B. Shah, Julia: A Fresh Approach to
599 Numerical Computing. *SIAM Rev.* **59**, 65–98 (2017).

600 38. A. Rakovic, D. Voß, F. Vulinovic, B. Meier, A.-K. Hellberg, C. Nau, C. Klein, E.
601 Leipold, Electrophysiological Properties of Induced Pluripotent Stem Cell-
602 Derived Midbrain Dopaminergic Neurons Correlate With Expression of Tyrosine
603 Hydroxylase. *Front. Cell. Neurosci.* **16** (2022).

39. P. Stathakos, N. Jimenez-Moreno, L. Crompton, P. Nistor, M. A. Caldwell, J. D. Lane, “Imaging Autophagy in hiPSC-Derived Midbrain Dopaminergic Neuronal Cultures for Parkinson’s Disease Research” in *Autophagy: Methods and Protocols*, N. Ktistakis, O. Florey, Eds. (Springer, New York, NY, 2019; https://doi.org/10.1007/978-1-4939-8873-0_17), pp. 257–280.

40. J. Louradour, O. Bortolotti, E. Torre, I. Bidaud, N. Lamb, A. Fernandez, J.-Y. Le Guennec, M. E. Mangoni, P. Mesirca, L-Type Cav1.3 Calcium Channels Are Required for Beta-Adrenergic Triggered Automaticity in Dormant Mouse Sinoatrial Pacemaker Cells. *Cells* **11**, 1114 (2022).

41. F. Philippart, G. Destreel, P. Merino-Sepúlveda, P. Henny, D. Engel, V. Seutin, Differential Somatic Ca2+ Channel Profile in Midbrain Dopaminergic Neurons. *J. Neurosci.* **36**, 7234–7245 (2016).

42. G. Destreel, V. Seutin, D. Engel, Subsaturation of the N-methyl-D-aspartate receptor glycine site allows the regulation of bursting activity in juvenile rat nigral dopamine neurons. *Eur. J. Neurosci.* **50**, 3454–3471 (2019).

43. S. Ringlet, Z. Motta, L. Vandries, V. Seutin, K. Jehasse, L. Caldinelli, L. Pollegioni, D. Engel, Glycine-gated extrasynaptic NMDARs activated during glutamate spillover drive burst firing in nigral dopamine neurons. *Prog. Neurobiol.* **249**, 102773 (2025).

44. L. Borgs, E. Peyre, P. Alix, K. Hanon, B. Grobarczyk, J. D. Godin, A. Purnelle, N. Krusy, P. Maquet, P. Lefebvre, V. Seutin, B. Malgrange, L. Nguyen, Dopaminergic neurons differentiating from LRRK2 G2019S induced pluripotent stem cells show early neuritic branching defects. *Sci. Rep.* **6**, 33377 (2016).

Acknowledgments

We thank our colleagues from the laboratories of Neuroengineering and Neurophysiology for their valuable input and help, especially L.Vandries for the histology of human mDANs. We thank our colleagues Pr. J-F Liégeois and Dr. R. Vitello for providing the mesylate salt of XG. We thank B. Fischer, J. Sonntag, S. Betz, G. Amrhein and T. Wulf for technical assistance in this project.

Funding

This work was supported by the Belgian Government through the Federal Public Service (FPS) Policy and Support (BOSA) grant NEMODEI (NEuroMOrphic Design of Embodied Intelligence) (AFy, JB, AFr, GD, KJ) ; Fonds National de la Recherche Scientifique (FNRS, Belgium) grants ASP-REN40024838 (AFy), J.0148.19 and T.0188.22 (VS). AFy is a Postdoctoral Researcher of FNRS. Liège University ; “Strategic opportunity grant” R.DIVE 1142-J-P-A-02 (OP, VS) ; Fondation Léon Frédéricq (KJ) ; Deutsche Forschungsgemeinschaft (DFG) - CRC1451 (JR).

Author contributions

Conceptualization: AFy, VS, GD & KJ; Methodology: AFy, SR, JB, AFr, KJ; Investigation: AFy, OP, NS, PM, & KJ; Visualization: AFy & KJ; Funding acquisition: VS, GD & KJ; Project administration: VS, GD & KJ; Supervision: JR, MM, VS, GD & KJ; Writing – original draft: AFy & KJ; Writing – review & editing: all authors

Competing interests

Authors declare that they have no competing interests.

Data and materials availability

All data and codes will be available upon publication.

655 **Figure legend**

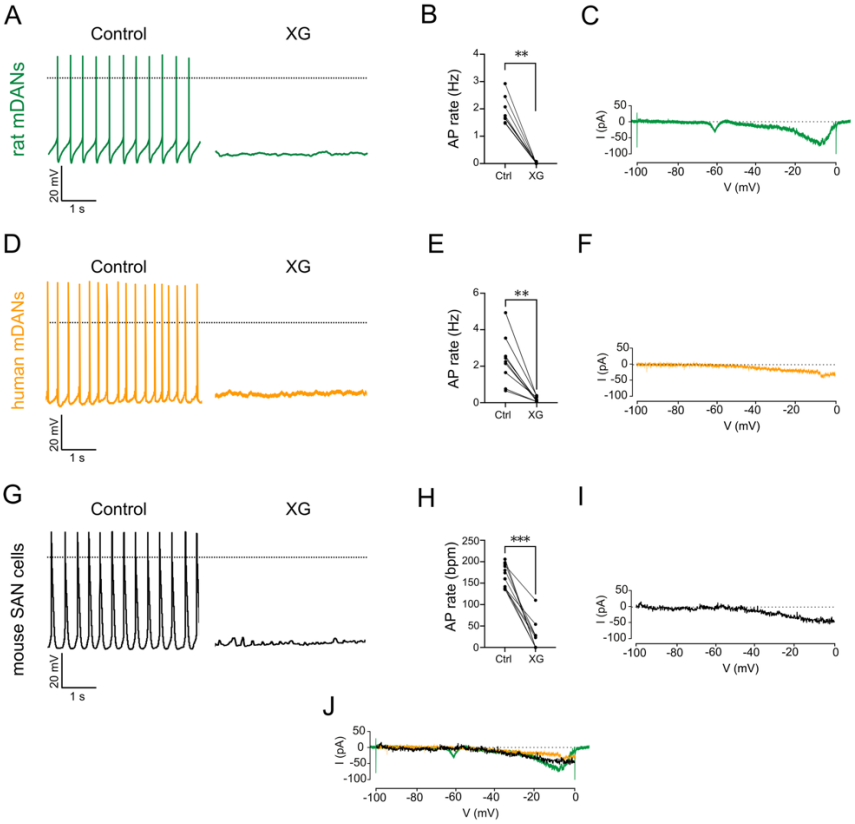

656

657 **Fig. 1. XG inhibits slow pacemaker cells.** (**A**) Pacemaking in rat mDANs is inhibited
658 upon (2 mM) XG application. (**B**) Summary data of the effect of the application of 2 mM
659 XG on the firing frequency. XG abolished the firing (1.94 ± 0.18 Hz in control vs 0.02 ±
660 0.001 Hz in XG, n = 8, p = 0.0078, Wilcoxon test). (**C**) XG-sensitive current isolated
661 from rat mDANs. Inward current at -60 mV is the result from rundown of T-type calcium
662 channels that was observed in one cell. (**A-C**) were adapted from *Jehasse et al. 2021*
663 (*6*). (**D**) Pacemaking in human mDANs is inhibited upon (600 µM) XG application. (**E**)
664 Summary data of the effect of the application of 600 µM XG on the firing frequency
665 (2.28 ± 0.44 Hz in control vs 0.12 ± 0.05 in XG, n = 9, p = 0.0039, Wilcoxon test). (**F**)
666 XG-sensitive current isolated from human mDANs (**G**) Pacemaking in mouse SAN
667 cells is inhibited upon (300 µM) XG application. (**H**) Summary data of the effect of the
668 application of 600 µM XG on the firing frequency, in beats per minute (bpm). XG
669 strongly reduces the firing (166.50 ± 9.11 bpm in control vs 24.55 ± 10.10 bpm in XG,
670 n = 11, p = 0.001, Wilcoxon test). (**I**) XG-sensitive currents isolated from mouse SAN
671 cells. (**J**) Overlay of XG-sensitive current from rat (green) and human mDANs (orange),
672 and SAN cells (black) shows similarities in voltage activation and current intensity.
673 Dashed lines correspond to 0 mV for voltage traces and 0 pA for current traces

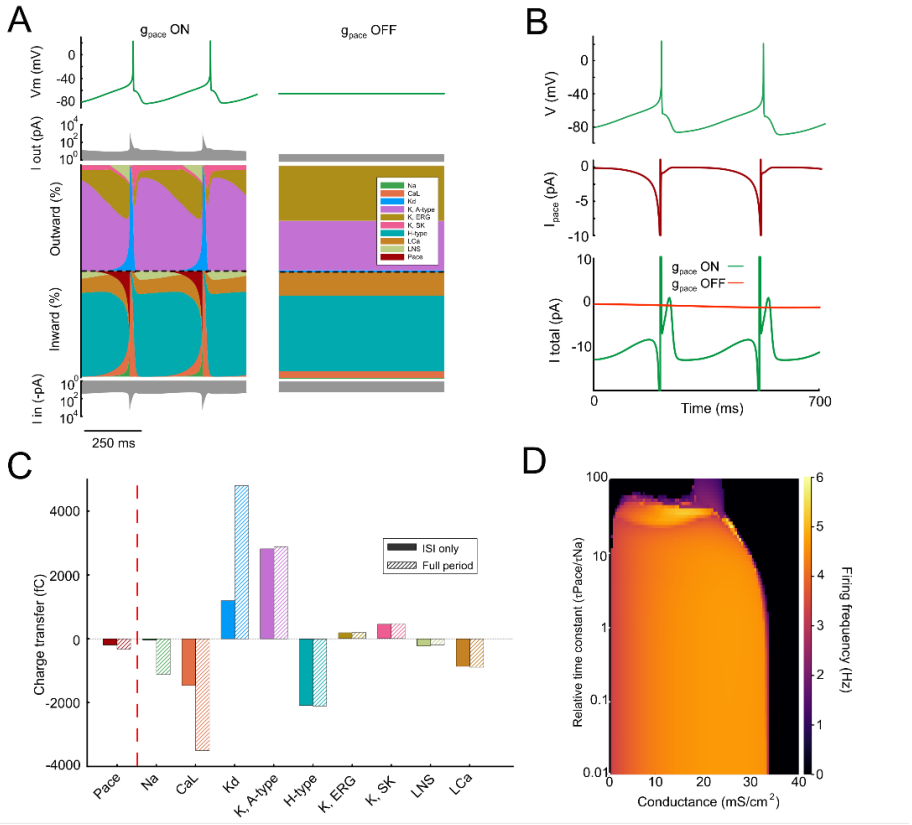

Fig. 2. Fast activating pacemaker conductance allows slow pacemaking in a mDAN conductance-based model. (**A**) Currentscape analysis reveals that, although its contribution seems small in comparison to other conductances, g_{pace} is crucial to generate slow pacemaking. (**B**) Simulated pacemaking activity in our adjusted pacemaking model (green) with I_{pace} dynamic below in red, showing a small amplitude during the interspike interval as previously observed (*6*). Bottom panel corresponds to total current amplitude from our adjusted model with (green) and without (red) the addition of g_{pace}. The total current observed is similar to what has been calculated (*10*). (**C**) Total charge transfer of each conductance during the interspike interval (ISI) and the full period of the simulation. Charge transfer was calculated by measuring the area under the curve in (**A**). (**D**) Heatmap analysis showing the multiplicative time constant of g_{pace} activation relative to g_{Na} according to the conductance density in which our adjusted model generates slow pacemaking.

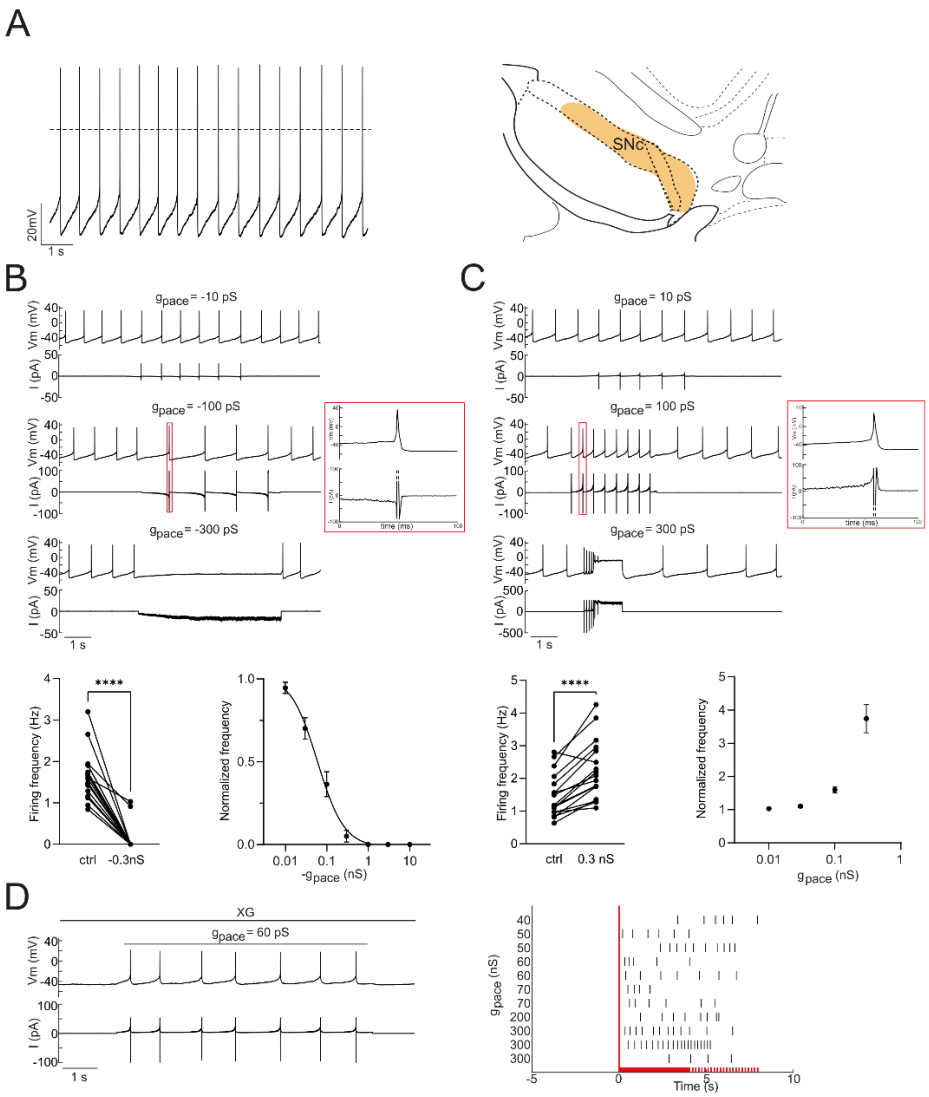

Fig. 3. The XG-sensitive conductance (g_{pace}) modulates pacemaking in *SNc* DANs. (**A**) *Ex vivo* pacemaking in a mouse *SNc* (orange shade) DAN. (**B**) Silencing of a *SNc* DAN upon injection of negative g_{pace} (upper panel). Summary data of the effect of negative g_{pace} on the firing frequency (lower panel). Negative g_{pace} abolished pacemaking at -0.3 nS (1,54 Hz (interquartile range: 1,193 - 1,864 Hz) in ctrl vs. 0 Hz (interquartile range: 0) with g_{pace} = - 0,3 nS, n = 20, N = 3, p = <0,0001, Wilcoxon test). (**C**) Excitation and overexcitation (depolarization block) of a *SNc* DAN upon positive g_{pace} (upper panel). Summary data of the effect of positive g_{pace} on the firing frequency (lower panel). g_{pace} increased the firing frequency (1,48 ± 0,66 Hz in ctrl vs. 2,26 ± 0,91 Hz with g_{pace} = 0,3 nS, n = 17, N =3, p = <0,0001, paired t test). (**D**) Rescue of pacemaking after preincubation with (2 mM) XG and complete cessation of pacemaking. Firing pattern and g_{pace} value upon rescue display broad large variability (right). Time frame of steady state g_{pace} (bold red line). Time frame of manual deactivation of g_{pace} (discontinuous red line).

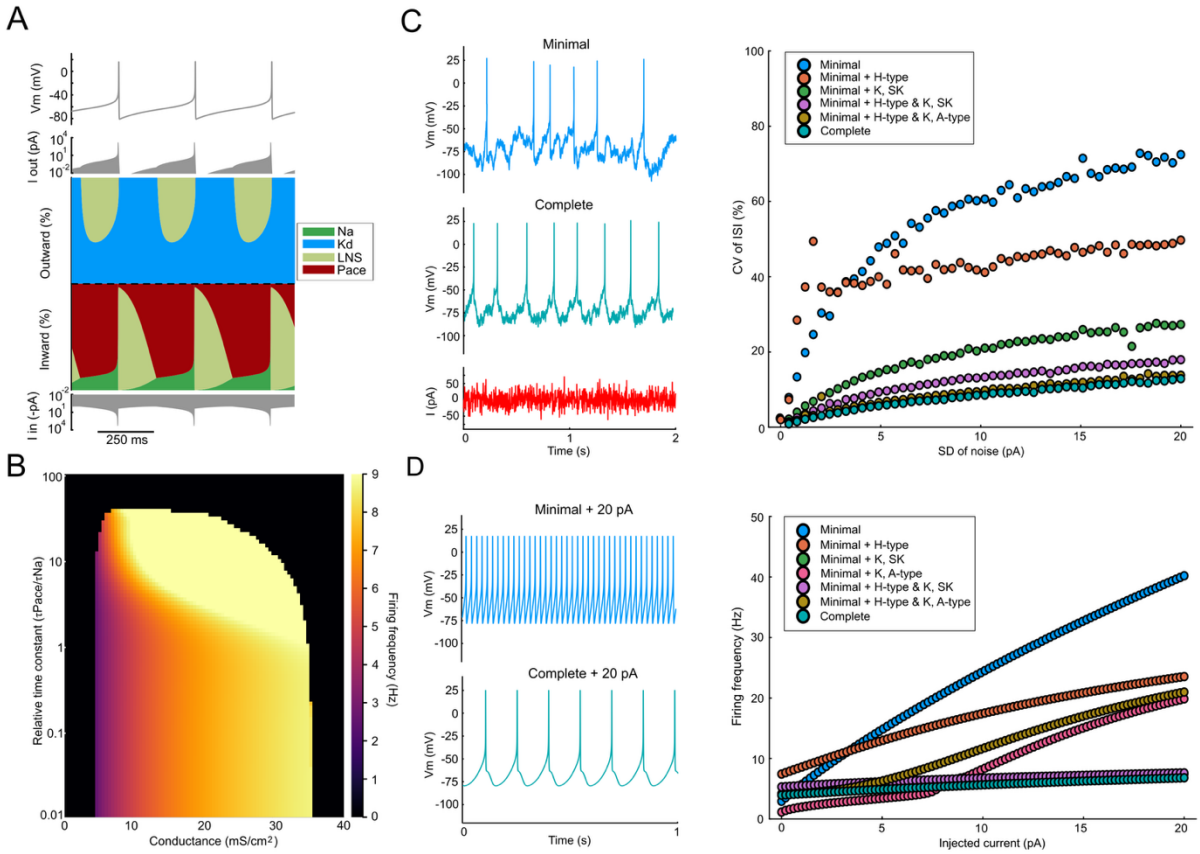

Fig. 4. Assessment of the conductances contribution in slow pacemaking. (**A**) Currentscape analysis from a minimal model including g_{Na}, g_{Kd}, g_{LNS} and g_{pace} shows that it is possible to generate slow pacemaking, similarly to what we observed *ex vivo* in the absence of other conductances (*6*), and that g_{pace} contribution is maximal during the interspike interval. (**B**) Heatmap analysis showing the multiplicative time constant of g_{pace} activation relative to g_{Na} according to the conductance density in which our minimal model generates slow pacemaking. (**C**) Robustness of slow pacemaking in response to noise (in red). In the minimal model (blue), current noise leads to irregular spiking, while the complete model (teal), current noise injection does not alter pacemaking regularity (left panel). Right panel corresponds to the effect of increasing the standard deviation (SD) of noise current to the coefficient of variation (CV) of the interspike interval (ISI). The addition of g_H, g_{KSK} and g_{KA} increases the robustness of slow pacemaking. In order to activate g_{KSK}, g_{LCa} was added. (**D**) Effect of the other conductances on the firing frequency upon continuous current injection. Left panel shows example of the firing frequency of the minimal (blue) and complete (teal) upon current injection of 20 pA. Right panel shows the effect of the combination of several conductances on the FI relationship. The results related to g_{KSK} addition only are located behind the complete and combination of g_{KSK} and g_H data points.

Supplementary figures

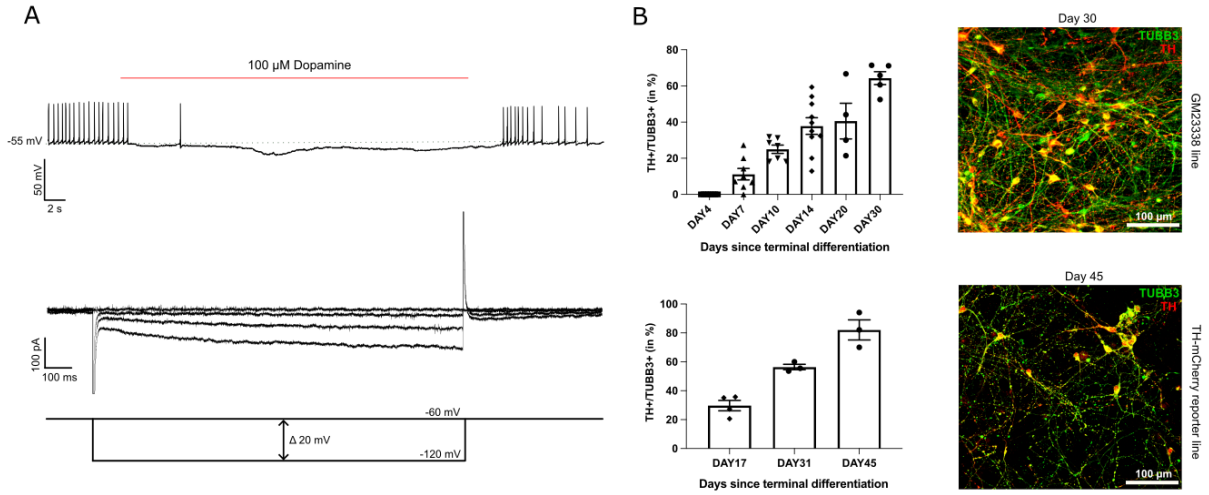

Fig. S1. Identification of human mDANs. (**A**) Top panel shows that application of dopamine on mDANs triggers silencing of pacemaking by hyperpolarization due the activation of DA autoreceptors (*44*), as observed in rodent mDANs (*41*). Bottom panel shows an example traces of I_H in human mDANs. (**B**) Evolution of the expression of TH, showing differentiation of neurons into mature mDANs.

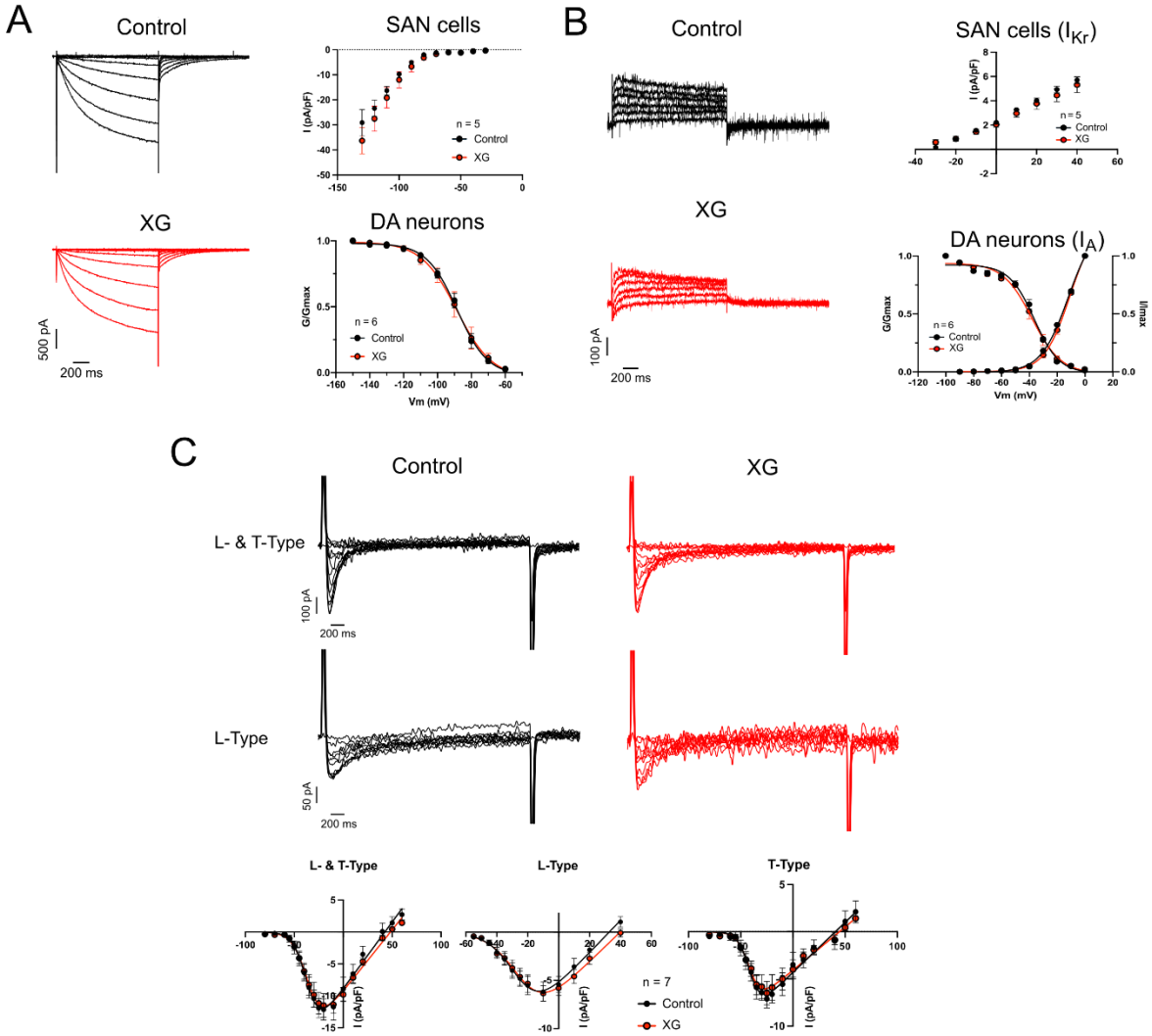

731

732 **Fig. S2. Slow pacemaking silenced by XG is not due to an off-target effect on the**
733 **main voltage-gated channels of SAN cells**. (**A**) XG does not interact with neuronal
734 and cardiac HCN currents. (**B**) XG interacts neither with delayed rectifier nor A-type
735 potassium channels. (**C**) XG does not decrease L-type and T-type calcium currents of
736 SAN cells. Graphs of mDANs were adapted from *Jehasse et al. 2021* (*6*).

737

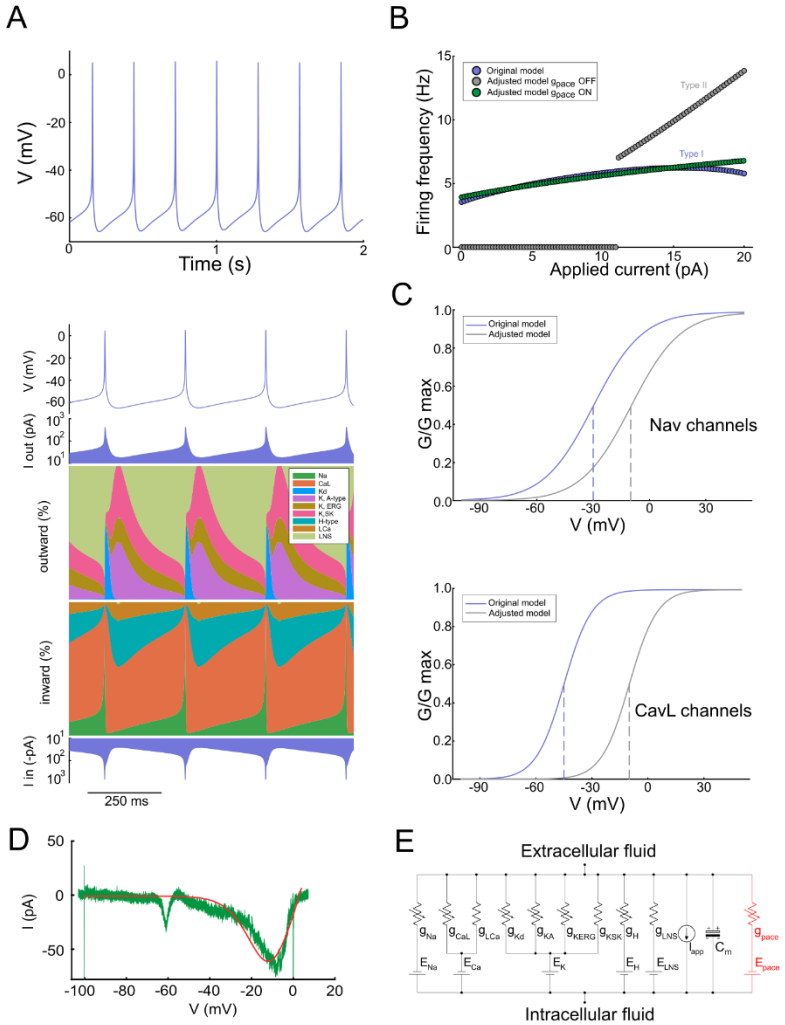

Fig. S3. Adjustment of current conductance-based model of a mDAN. (**A**) Simulated pacemaking and currentscape analysis from the model of *Yu et Canavier 2015* (*12*). (**B**) Blue dots represent the firing frequency relative to current injections from the model of Yu et Canavier, showing a type I excitability similar to in vitro mDANs. Grey dots represent the firing frequency relative to current injections from the adujsted model of *Yu et Canavier*, changing the excitability type from I to II. Adding g_{pace} to the adjusted model (green dots) shifts the excitability of the neuron from type II to type I. (**C**) Activation curves from Na_v (top) and L-type Ca_v (bottom) channels. Blue curves correspond to the parameters used in the model of *Yu et Canavier*, while grey curves corresponds to our adjustment to physiological values as observed in mDANs for Na_v (*14*) and L-type Ca_v channels (*15*). (**D**) Fitting curve (red) based on XG-sensitive current (green) to generate g_{pace}. (**E**) Circuit for conductance-based model with nonlinear conductances and the pacemaking conductance (in red).

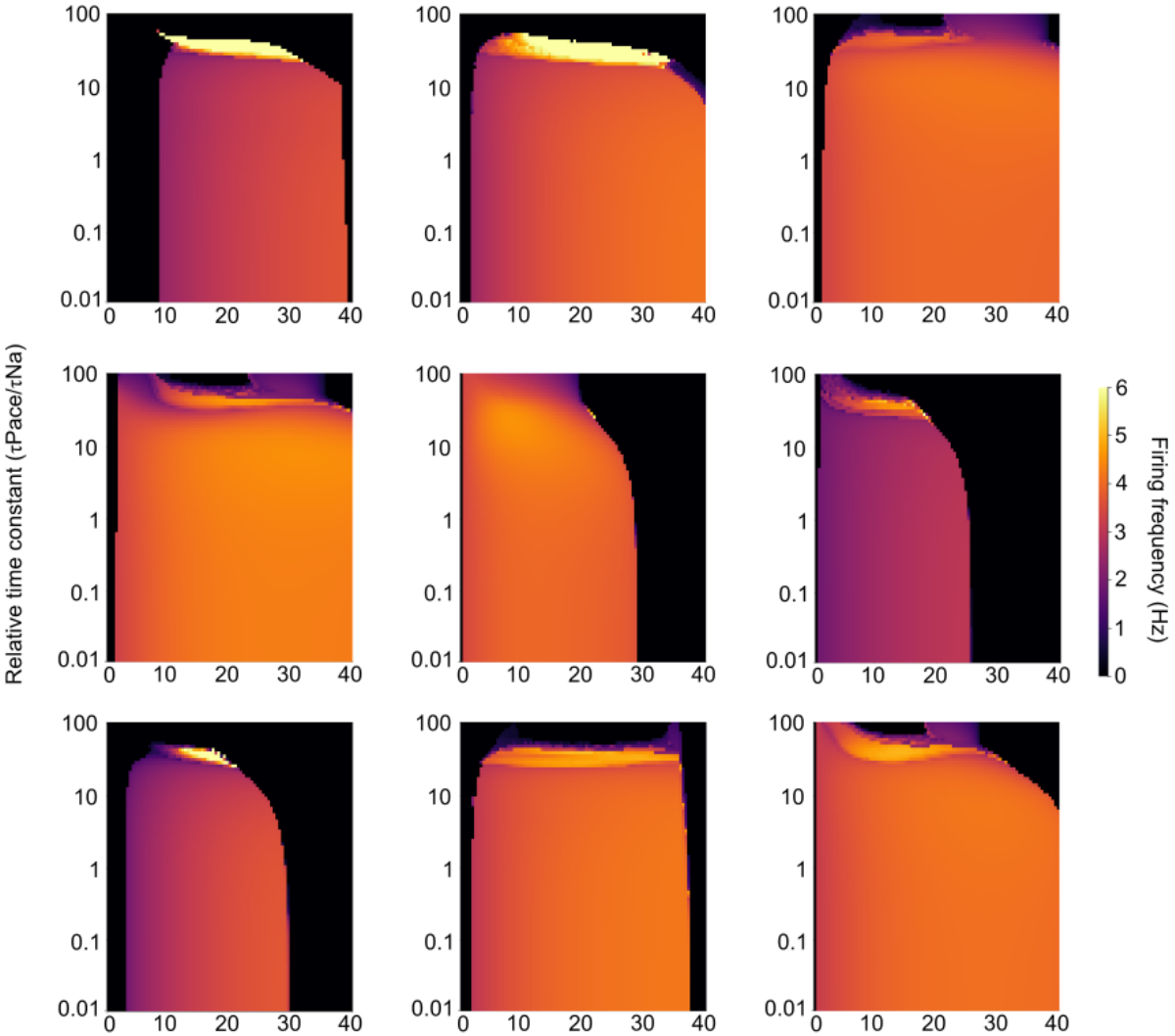

Fig. S4. Additional heatmaps generated from other random conductance values for all channels. Overall, we observe a wide range of densities from g_{pace} in order to produce slow pacemaking, with fast kinetics.

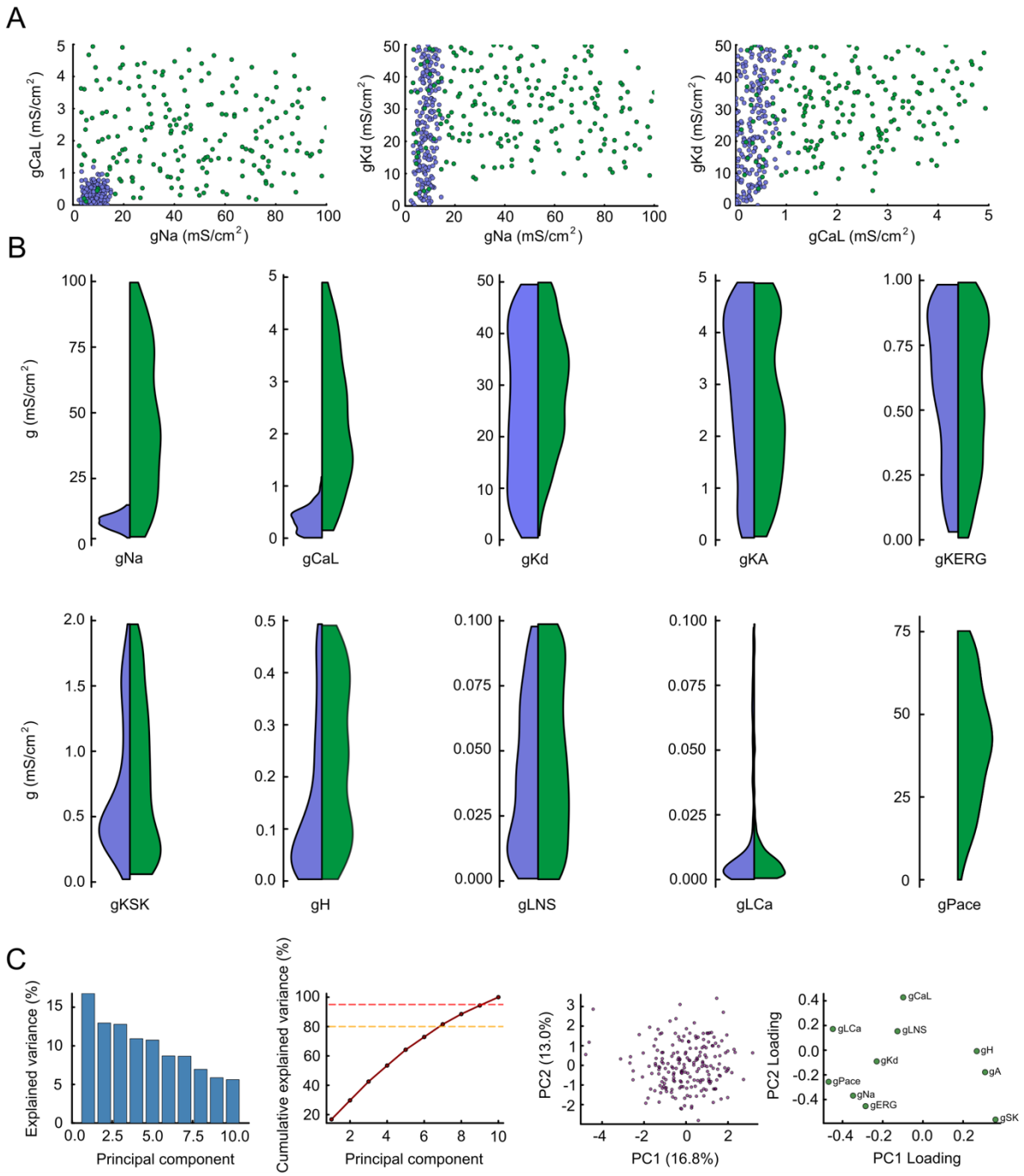

Fig. S5. Degenerate populations and PCA analysis of the adjusted model. (**A**) Scatter plots of degenerate populations for the original (blue) and adjusted (green) models in selected conductance subspaces (g_{Na}, g_{CaL} and g_{Kd}), highlighting that our model allows more degeneracy. (**B**) Violin plots of all conductances for both populations. (**C**) Summary of PCA analysis on the adjusted degenerate population (green in **A** and **B**). From left to right: bar plot of explained variance for each component, scree plot, projection onto the PC1–PC2 plane, and scatter plot of PC1/PC2 loadings.

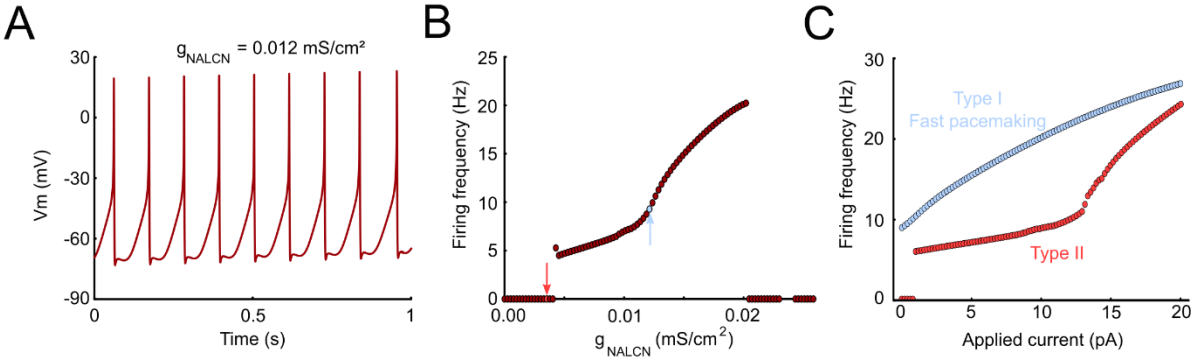

Fig. S6. Voltage-dependence of g_{pace} is required to generate steady and slow pacemaking. (**A**) Replacement of g_{pace} by a linear depolarizing conductance in our adjusted model such as g_{NALCN} does not result in slow pacemaking. (**B**) Firing frequency related to the density of g_{NALCN} shows the restricted range of g_{NALCN} density where pacemaking occurs. (**C**) Firing frequency – current relationship curve shows that low density of g_{NALCN} leads to type II excitability, which does not correspond to mDANs excitability, whereas higher density of g_{NALCN} leads to type I fast pacemaking, also not corresponding to mDANs slow firing frequency.

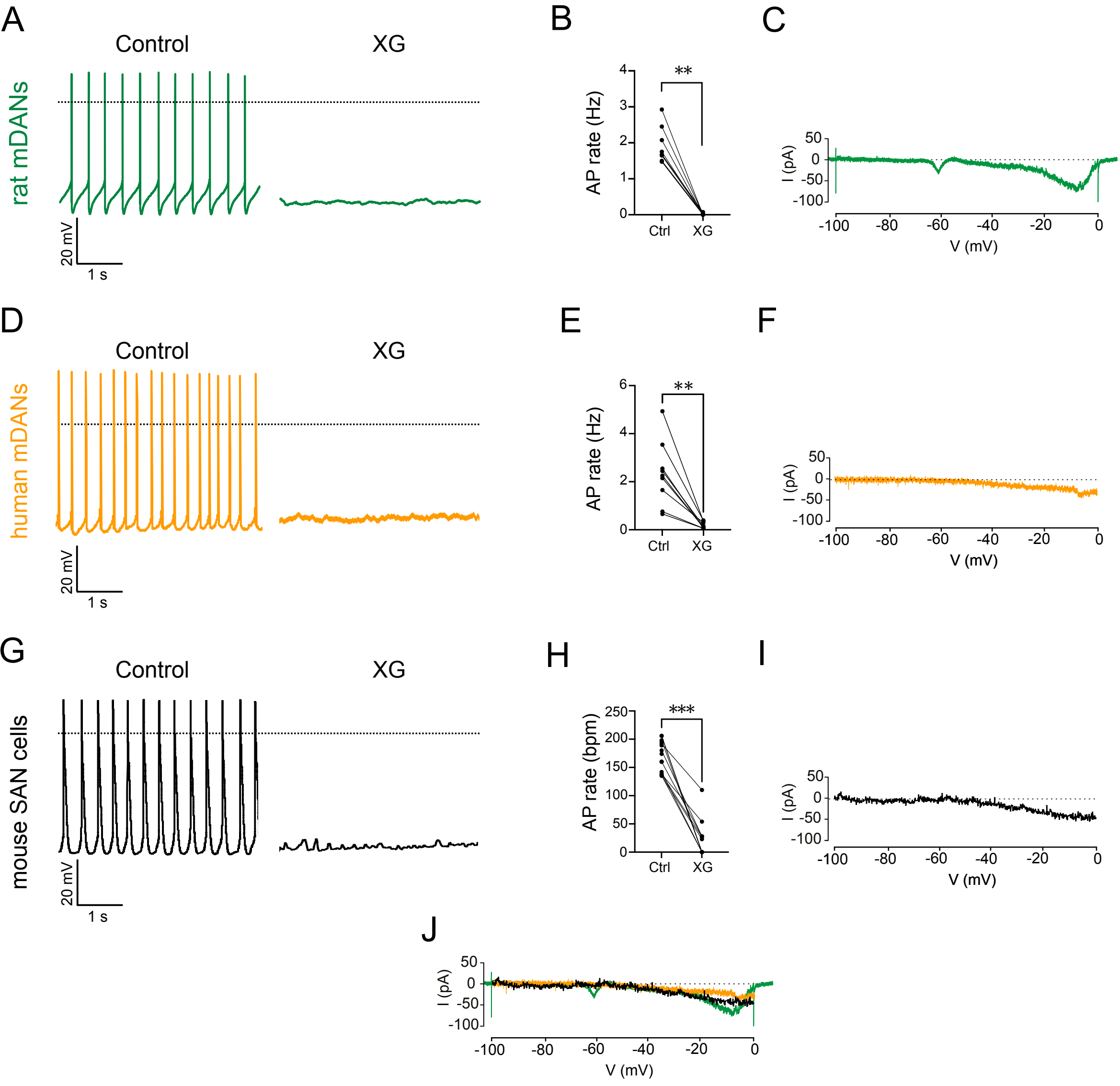
A
Control
XG
rat mDANs
20 mV
1 s
B
AP rate (Hz)
**
Ctrl
XG
C
I (pA)
V (mV)
D
Control
XG
human mDANs
20 mV
1 s
E
AP rate (Hz)
**
Ctrl
XG
F
I (pA)
V (mV)
G
Control
XG
mouse SAN cells
20 mV
1 s
H
AP rate (bpm)
***
Ctrl
XG
I
I (pA)
V (mV)
J
I (pA)
V (mV)

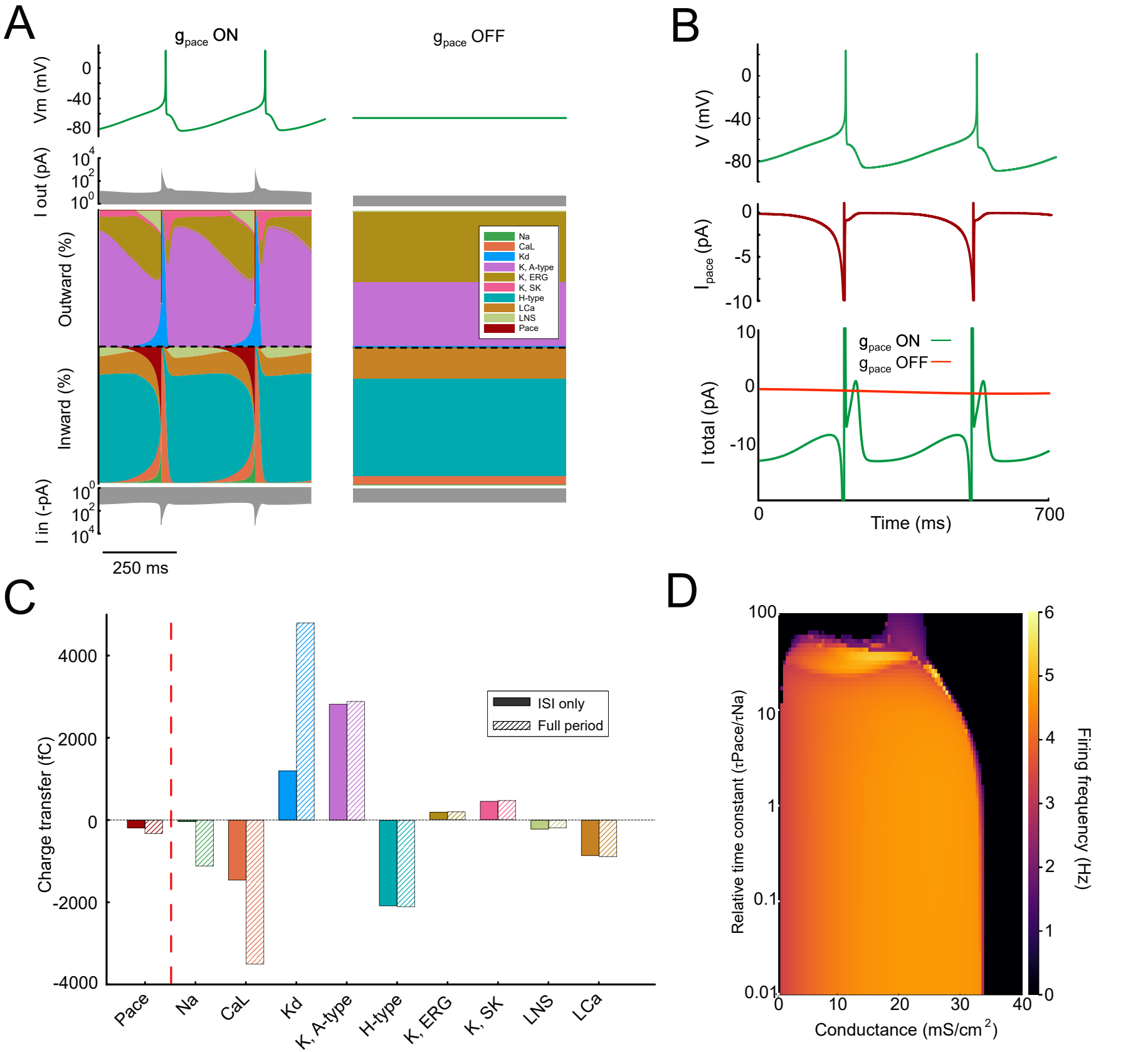
A
g_{pace} ON
g_{pace} OFF
Vm (mV)
0
-40
-80
I out (pA)
10^4
10^2
10^0
Outward (%)
Inward (%)
I in (-pA)
10^0
10^2
10^4
250 ms
Na
CaL
Kd
K, A-type
K, ERG
K, SK
H-type
LCa
LNS
Pace
B
V (mV)
0
-40
-80
I_{pace} (pA)
0
-5
-10
I total (pA)
10
0
-10
g_{pace} ON
g_{pace} OFF
0
Time (ms)
700
C
Charge transfer (fC)
4000
2000
0
-2000
-4000
ISI only
Full period
Pace
Na
CaL
Kd
K, A-type
H-type
K, ERG
K, SK
LNS
LCa
D
Relative time constant (τPace/τNa)
100
10
1
0.1
0.01
0
10
20
30
40
Conductance (mS/cm^2)
Firing frequency (Hz)
6
5
4
3
2
1
0

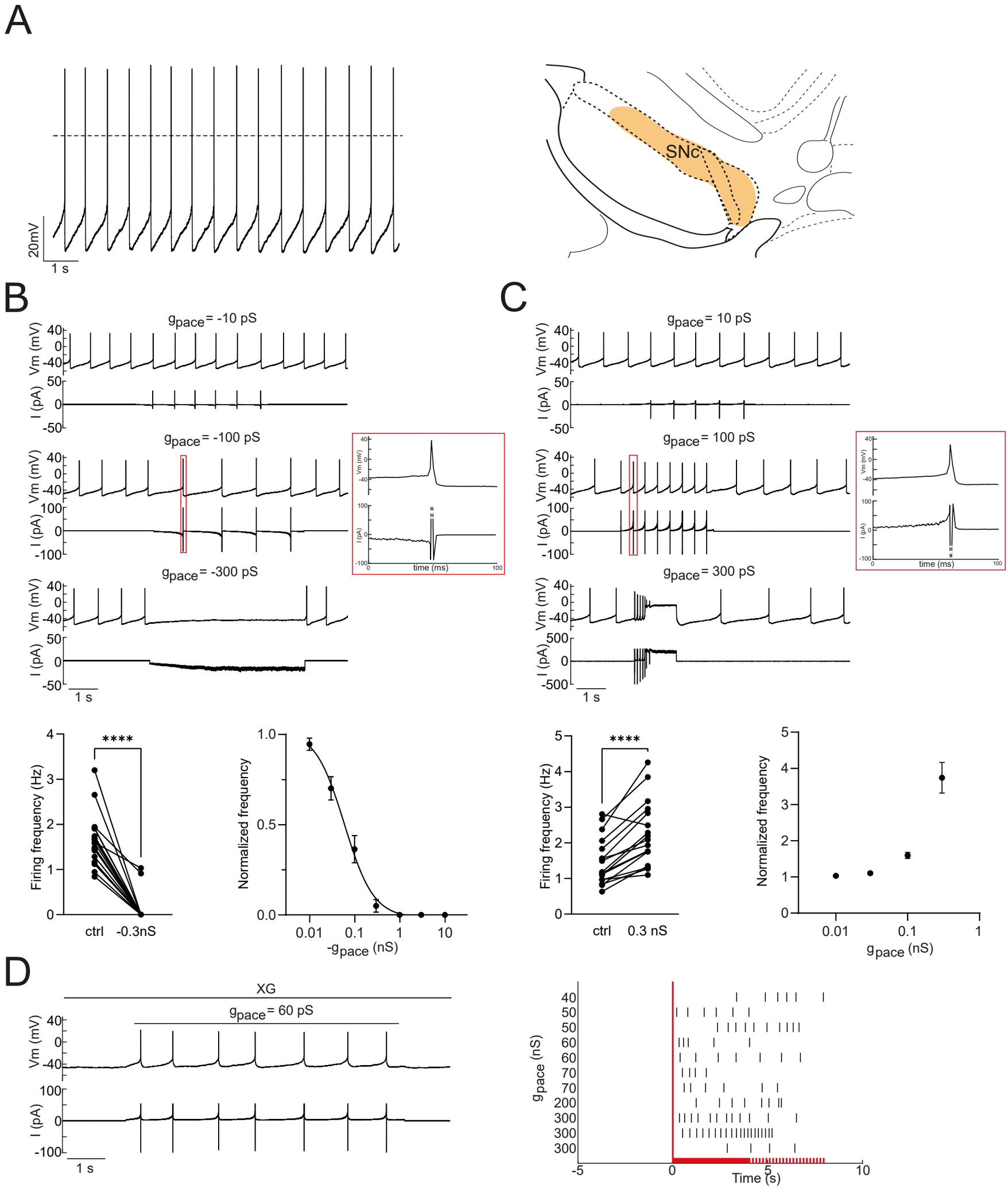
A
20mV
1 s
SNc
B
gpace= -10 pS
gpace= -100 pS
gpace= -300 pS
Vm (mV)
I (pA)
time (ms)
1 s
****
Firing frequency (Hz)
ctrl
-0.3nS
Normalized frequency
-gpace (nS)
C
gpace= 10 pS
gpace= 100 pS
gpace= 300 pS
0.3 nS
gpace (nS)
D
XG
gpace= 60 pS
Time (s)

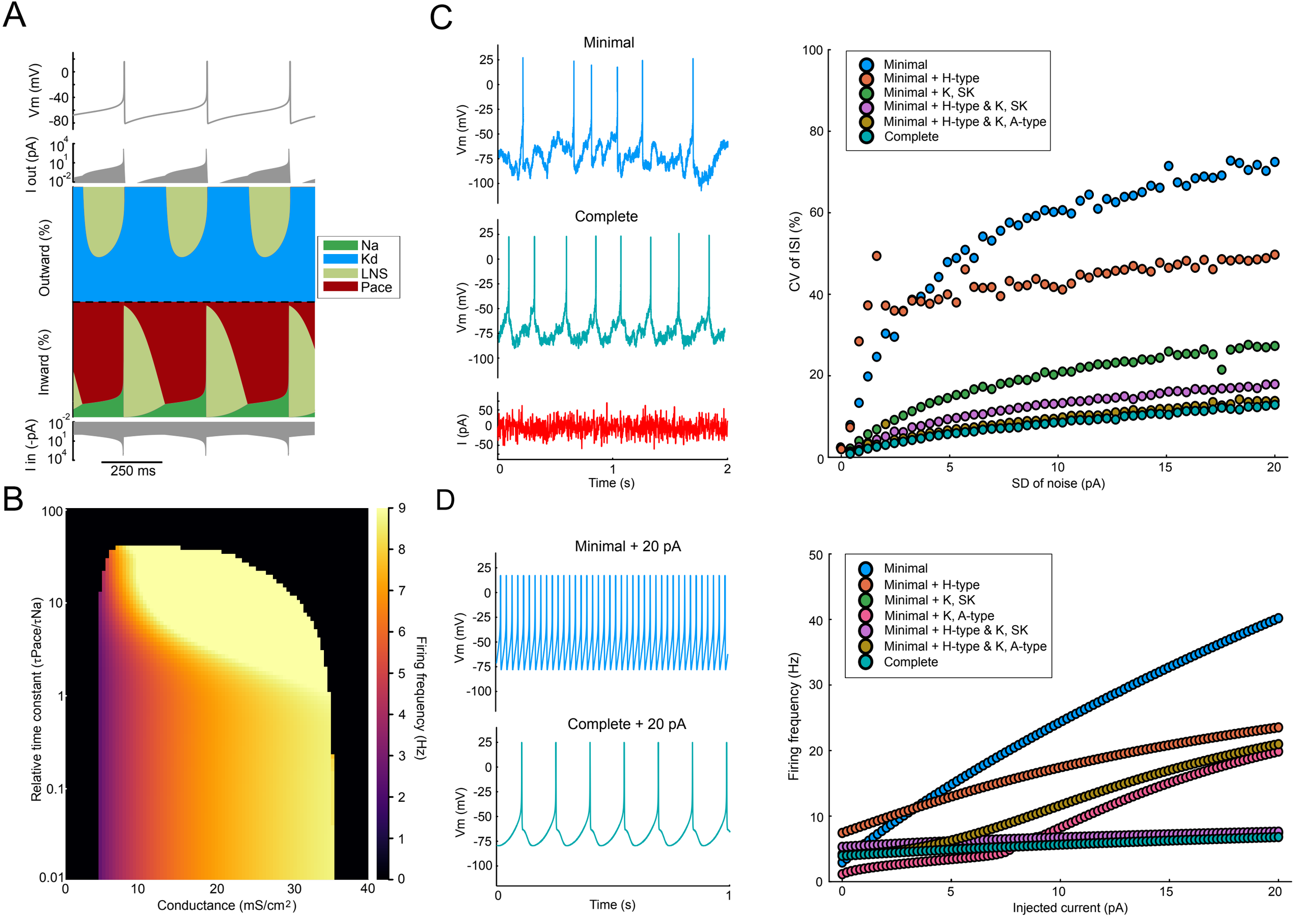
A
Vm (mV)
0
-40
-80
I out (pA)
10^4
10^1
10^{-2}
Outward (%)
Inward (%)
Na
Kd
LNS
Pace
I in (-pA)
10^{-2}
10^1
10^4
250 ms
B
Relative time constant (τPace/τNa)
100
10
1
0.1
0.01
0
10
20
30
40
Conductance (mS/cm²)
Firing frequency (Hz)
9
8
7
6
5
4
3
2
1
0
C
Minimal
Vm (mV)
25
0
-25
-50
-75
-100
Complete
I (pA)
50
0
-50
0
1
2
Time (s)
CV of ISI (%)
100
80
60
40
20
0
Minimal
Minimal + H-type
Minimal + K, SK
Minimal + H-type & K, SK
Minimal + H-type & K, A-type
Complete
0
5
10
15
20
SD of noise (pA)
D
Minimal + 20 pA
Complete + 20 pA
Time (s)
1
Firing frequency (Hz)
50
40
30
20
10
0
Minimal
Minimal + H-type
Minimal + K, SK
Minimal + K, A-type
Minimal + H-type & K, SK
Minimal + H-type & K, A-type
Complete
Injected current (pA)